Journal of Magnetic Resonance 305 (2019) 185–194

Contents lists available at ScienceDirect

Journal of Magnetic Resonance

journal homepage: www.elsevier.com/locate/jmr

Accelerated imaging with segmented 2D pulses using parallel imaging and virtual coils

Michael Mullen [a,b], Alexander Gutierrez [c], Naoharu Kobayashi [a], Jarvis Haupt [d], Michael Garwood [a,*]

[a] Center for Magnetic Resonance Research, Department of Radiology, University of Minnesota, Minneapolis, MN, USA
[b] School of Physics and Astronomy, University of Minnesota, Minneapolis, MN, USA
[c] School of Mathematics, University of Minnesota, Minneapolis, MN, USA
[d] Department of Electrical and Computer Engineering, University of Minnesota, Minneapolis, MN, USA

ARTICLE INFO

Article history:
Received 30 April 2019
Revised 2 July 2019
Accepted 3 July 2019
Available online 4 July 2019

Keywords:
MRI
B_0 inhomogeneity
2D pulse
Segmented pulse
Frequency-modulated
Parallel imaging
GRAPPA
Virtual coil

ABSTRACT

Large magnetic field inhomogeneity can be a significant cause of spatial flip-angle variation when using ordinary, limited-bandwidth RF pulses. Multidimensional RF pulses are particularly sensitive to inhomogeneity due to their extended pulse length, which decreases their bandwidth. Previously, it was shown that, by breaking a 2D pulse into multiple undersampled k-space segments, the excitation bandwidth can be increased at the expense of increased imaging time. The present study shows how this increased imaging time can be offset by undersampling acquisition k-space in a phase-encoded dimension that is in the direction of excitation segmentation. Data from each segment are viewed as originating from "virtual receive coils" rather than multiple physical coils. The undersampled data are reconstructed using parallel imaging techniques (e.g. as in GRAPPA). The method was tested in vivo with brain imaging at both 3 T and 4 T, and used in conjunction with a 32-channel head coil and conventional GRAPPA on the 3 T data. Relationships with existing techniques and future applications are discussed.

1. Introduction

Previous work has shown how the k-space trajectory of a multidimensional radiofrequency (RF) pulse [1–5] can be segmented and acquired in separate shots. In the absence of segmenting, multidimensional RF pulses suffer from a low bandwidth due to the long pulse lengths necessary for full sampling. Undersampling of excitation k-space permits a shorter pulse length and increased pulse bandwidth; however, in MRI applications of segmented 2D and 3D pulses, the need to fully sample acquisition k-space per excitation segment leads to longer scans, since the imaging time increases linearly with the number of pulse segments used. This requirement decreases the utility of this approach. Alternatively, as described by Norris et al. [6], the effective bandwidth can be increased by multiplying the pulse by a Dirac comb. By this approach, the effective bandwidth increases due to the production of sidebands, which may not be ideal for certain applications such as 3D inner volume imaging.

Segmenting multidimensional pulses is useful whenever multidimensional localization is desired with robustness to B_0 inhomogeneity. Examples include localized spectroscopy [4,7,8] and inner volume imaging [9,10]. For sequences with an EPI readout, the reduced field-of-view (FOV) resulting from using a multidimensional pulse permits shorter echo-trains, thereby diminishing distortions in regions with large susceptibility differences [10]. Segmenting the excitation pulse in these cases would increase the excitation bandwidth, yielding a more robust excitation profile.

Signals produced by each excitation segment contain independent information although the same object is being imaged while using the same transmit and receive coil(s). This is due to various spatial phases resulting per excitation with the different pulse segments. In previous work [1], the acquired data for all pulse segments were fully sampled prior to a weighted, complex summation of the data. Here, it is shown that the redundancy between pulse segments permits data undersampling in the phase-encoded dimension aligned with the segmented dimension of the pulse. The data can then be reconstructed using Generalized Autocalibrating Partially Parallel Acquisitions (GRAPPA) [11] and potentially other parallel imaging techniques. This approach is made possible by treating the data from each pulse segment as if received by a virtual coil with a spatially dependent sensitivity map. The total number of virtual coils is then equal to the number of excitation segments used, provided there is only one receive coil.

* Corresponding author.
E-mail address: gar@cmrr.umn.edu (M. Garwood).

https://doi.org/10.1016/j.jmr.2019.07.001
1090-7807/

The notion of virtual coils was introduced by Blaimer et al. [12], in which synthetic, conjugated data from an undersampled Cartesian acquisition was treated as if originating from a virtual coil. A similar approach to accelerate acquisition when using more than one type of excitation was taken by Orzada et al. [13], using a technique named Time Interleaved Acquisition of Modes (TIAMO). There, the transmit coil was driven in two different excitation modes, with the data being undersampled on acquisition for both modes and reconstructed using GRAPPA. This resulted in two virtual receive coils. In the new method described here, the transmit coil operates in the same excitation mode for all pulses, instead using undersampled pulse segments for additional spatial encoding to accelerate data acquisition. The current work also permits a zoomed FOV in two dimensions. However, the reconstruction frameworks of the two approaches are similar, with some differences that will be thoroughly discussed in the next section and in the discussion.

2. Theory

When using a 2D RF pulse that has been segmented to achieve increased excitation bandwidth, the FOV can be reduced in the two spatially-selected dimensions, as with the fully-sampled, single-shot 2D pulse. To avoid an increase in imaging time, previous work [1] relied on the condition that the number of pulse segments not exceed the acceleration gained by using a reduced FOV. This condition is no longer strictly necessary, as the different pulse segments induce their own spatial modulation. The data from each excitation segment are then used to synthesize unsampled data in an accelerated acquisition. This concept is motivated by considering the excitation profile following a given pulse segment and the signal received following that excitation, neglecting relaxation effects. Assuming a small tip angle excitation [14], the magnetization profile $P(\vec{r})$ of the imaged object $I(\vec{r})$following pulse segment j is given by

$$P_j\left(\vec{r}\right) \propto i\gamma I\left(\vec{r}\right) \int_0^{T_p} B_{1,j}^{+}\left(\vec{r},t\right) \exp\left(i\vec{r}\cdot\vec{k}_j(t)\right)dt. \tag{1}$$

Here, $B_{1,j}^{+}(\vec{r},t)$ is the total complex RF field at position $\vec{r}$ and time t, γ is the proton gyromagnetic ratio, T_p is the RF pulse duration, and $\vec{k}_j(t)$ is a parameterized trajectory through excitation k-space for pulse segment j. The index j runs from 1, …,N_s, where N_s is the number of pulse segments used. Using the separability in space and time of the transmit field, that is, $B_{1,j}^{+}(\vec{r},t) = B_{1,j}^{+}(\vec{r})B_{1,j}^{+}(t)$, Eq. (1) can be rewritten as

$$P_j\left(\vec{r}\right) \propto i\gamma I\left(\vec{r}\right)B_{1,j}^{+}\left(\vec{r}\right) \int_0^{T_p} B_{1,j}^{+}(t) \exp\left(i\vec{r}\cdot\vec{k}_j(t)\right)dt. \tag{2}$$

The result of the integral is a function of position, $\vec{r}$, only, so Eq. (2) can be rewritten as

$$P_j(\vec{r}) \propto i\gamma I(\vec{r})B_{1,j}^{+}(\vec{r})M_j(\vec{r}), \tag{3}$$

where

$$M_j\left(\vec{r}\right) \triangleq \int_0^{T_p} B_{1,j}^{+}(t) \exp\left(i\vec{r}\cdot\vec{k}_j(t)\right)dt. \tag{4}$$

Now consider the signal, $S_{m,j}$, received in coil m following excitation by pulse segment j during signal acquisition. The index m is in the range 1, …,N_c, where N_c is the number of physical coils used. When using a spatially dependent receive field $B_1^{-}(\vec{r})$, the signal can be written as

$$S_{m,j}\left(\vec{k}_a(t)\right) \propto \int_V B_{1,m}^{-}\left(\vec{r}\right)P_j\left(\vec{r}\right) \exp\left(-i\vec{r}\cdot\vec{k}_a(t)\right)d\vec{r}. \tag{5}$$

The subscript a denotes acquisition, and the integral is performed over the sensitive volume V of the receive coil. Inserting the definition of P_j from Eq. (3), the signal is recast as

$$S_{m,j}\left(\vec{k}_a(t)\right) \propto i\gamma \int_V B_{1,m}^{-}\left(\vec{r}\right)M_j\left(\vec{r}\right)B_{1,j}^{+}\left(\vec{r}\right)I\left(\vec{r}\right) \exp\left(-i\vec{r}\cdot\vec{k}_a(t)\right)d\vec{r}. \tag{6}$$

By defining the spatially dependent quantity as

$$B_{m,j}(\vec{r}) \triangleq i\gamma B_{1,j}^{+}(\vec{r})B_{1,m}^{-}(\vec{r})M_j(\vec{r}), \tag{7}$$

the signal equation becomes

$$S_{m,j}(\vec{k}_a(t)) \propto \int_V B_{m,j}(\vec{r})I(\vec{r})exp(-i\vec{r}\cdot\vec{k}_a(t))d\vec{r}. \tag{8}$$

From Eqs. (7) and (8), the quantity $B_{m,j}$ can clearly be interpreted as a complex coil sensitivity profile. As discussed in [13], this is equivalent to assuming homogeneous excitation followed by Fourier and sensitivity encoding. Here, however, the virtual coil profile is the product of the physical receiver sensitivity, transmit field map, and pulse segment excitation profile, which distinguishes it from TIAMO. There, the virtual profile is the product of the physical receive sensitivity and transmit field map only. It is immediately apparent that even when only one physical receive coil is present, there are still N_s virtual coils to work with. When an N_s-segment pulse is combined with standard GRAPPA, the data from each pulse segment acquired with one physical coil can be split into N_s virtual coil data sets. Hence, the number of effective coils, N_c, is equal to the product N_sN_c, as seen from Eq. (7).

When using segmented pulses with N segments, Mullen et al. [1] noted the signal-to-noise ratio (SNR) for a N-segment pulse with respect to a single-shot pulse with N averages decreases as

$$\frac{\mathrm{SNR}_{\mathrm{segmented}}}{\mathrm{SNR}_{\mathrm{single-shot}}} = \frac{\sum_{j=1}^{N}|C_j|}{\sqrt{N\sum_{j=1}^{N}|C_j|^2}}. \tag{9}$$

with C_j defined as

$$C_j = \max\left|\int_0^T \omega_{1,j}(t)exp(-i\phi_{RF,j}(t))exp\left(i\vec{r}\cdot\vec{k}_j(t)\right)dt\right|. \tag{10}$$

Here, the subscript j denotes segment number and i the square root of −1. The C_j are weighting coefficients used in the pulse segment combination and were originally defined in [1]. Note that the equation presented previously omitted the term incorporating the k-space trajectory [15]. In Eq. (10), each C_j is set equal to the maximum value of the integral across all space $\vec{r}$, but other scaling prescriptions could be used, such as the mean value of each segment's magnetization profile.

When partially segmenting a 2D pulse, the flip angle at each spatial location varies from segment to segment, and the amount of variation is spatially dependent and increases with number of segments used, except when using the fully segmented pulse. With the commonly employed condition TR << T_1, variable T_1-weighting of the different segments cannot be ignored. The coefficients C_j are thus used to scale the peak RF amplitude to obtain a more consistent flip angle across pulse segments. This procedure requires a processing step to compensate for the increased flip angles from scaling, so that signal outside the region of interest is perfectly cancelled when summing over segments. By scaling the amplitude of each pulse segment, flip angle variations are minimized enough to avoid noticeable image artifacts.

However, undersampling the data using an effective acceleration R decreases the SNR by $\sqrt{R}$ relative to an unaccelerated acquisition [16]. Combining Eq. (9) with Eq. (5) of [16], the ratio of the SNR for a segmented 2D excitation, accelerated readout dataset to that of the equivalent sequence with a single-shot coverage of 2D excitation k-space and an unaccelerated readout is given by

$$\frac{\mathrm{SNR}_{\mathrm{segmented,accelerated}}}{\mathrm{SNR}_{\mathrm{single-shot,unaccelerated}}} = \frac{\sum_{j=1}^{N}|C_j|}{g\sqrt{NR\sum_{j=1}^{N}|C_j|^2}}, \tag{11}$$

where g is the g-factor map, an indication of noise amplification due to noise correlations.

3. Simulations

Simulations were performed to demonstrate the spatial modulation of transverse magnetization profiles of each pulse segment, which act as virtual coil profiles. For the first set of simulations, and in the experiments at 4T, identical excitation k-space parameters were used as in [1]. There, the 2D pulse was a 2D hyperbolic secant (HS1), with a time bandwidth product (TBP) equal to 9 in both dimensions, slab thickness = 5 cm, 28 total lines of excitation k-space, and subpulse durations of 700 μs. With 4 excitation segments, each segment traversed 7 lines of excitation k-space, with the same initial direction for each segment. The second 2D pulse

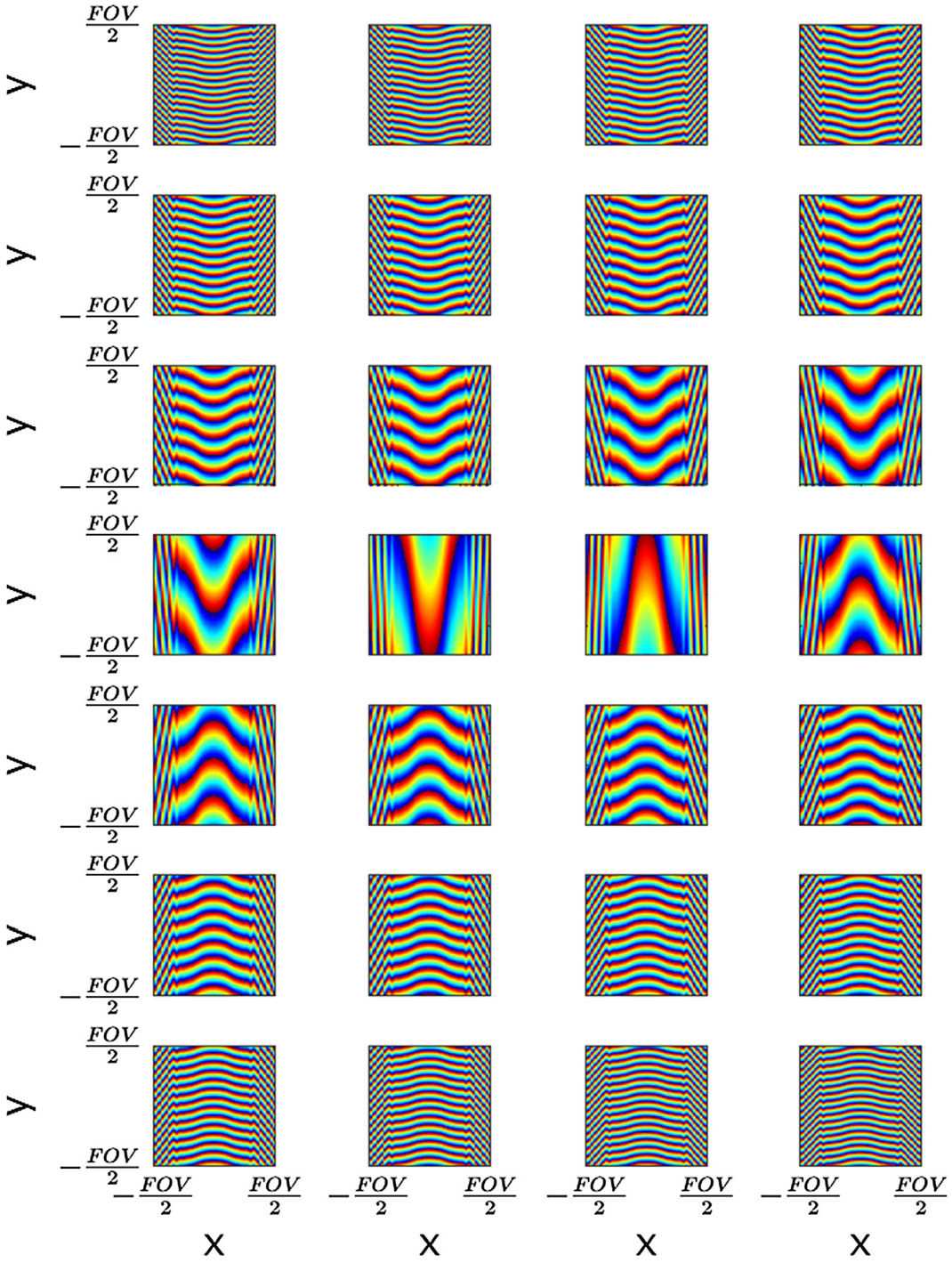

Fig. 1. The phase of the transverse magnetization for each of the 2D excitation segments when fully segmented into 28 pulse segments. The pulse parameters are described in the text. The x dimension is the fast (unsegmented) dimension of the pulse, while y is the slow (segmented) dimension of the pulse.

simulated, which was used experimentally at 3T, had the following parameters: $TBP_{fast} = 16$, $TBP_{slow} = 10$, and slab thickness in the slow and fast dimensions equal to 9 cm and 3.6 cm, respectively. A total of 20 lines of excitation k-space were sampled in the slow dimension, where each subpulse duration was 800 μs. Excitation k-space was sampled on the gradient ramps using VERSE [17] to shorten the pulse duration further. As discussed in [1], the flip angle of each pulse segment must be kept the same to maintain consistent T_1 weighting. The peak transmit field, B_1^{max}, to achieve the desired flip angle was determined by integration for each segment of the pulse. Data were recombined following the procedure in [1].

As can be seen in Fig. 1, in the case of the fully-segmented pulse with the pulse parameters used at 4T, the virtual coil profiles form a spatial-encoding basis set in one dimension, permitting higher undersampling factors in the segmented dimension of the pulse.

The phases of the transverse magnetizations produced with the 4-segment pulse are shown in Fig. 2. Although the spatial modulation of the magnetization phase in this case is less than that of the fully segmented case, the spatial modulation afforded is sufficient to permit a limited amount of acquisition undersampling.

To evaluate off-resonance effects for both 4-segment pulses used in experiments, the excitation profiles were simulated over a range of constant frequency offsets using an in-house Bloch simulator. These results are presented in Fig. 3. The excitation profile in the fast dimension (x) of the pulse is clearly improved, while this is not evident in the slow dimension (y) of the pulse. For the 4-segment pulse used at 3T, the behavior in the slow dimension of the pulse is worse than for the 4-segment pulse at 4T due to using a lower k_{max} in the slow dimension of the pulse, by nearly a factor of two. This leads to a higher sensitivity to off-resonance effects. Equivalent simulations for the fully segmented pulse are simulated and discussed in detail elsewhere [1].

4. Materials and methods

The performance of the 2D pulse acceleration method was tested in human brain imaging experiments using 4T Varian and 3T Siemens MRI scanners. The different RF hardware of these MRI systems (i.e., the different numbers of receiver coils and channels) allowed the acceleration method to be tested without (4T) and with (3T) conventional parallel acquisition. A protocol approved by our Institutional Review Board (IRB) was followed for human brain imaging of healthy volunteers after obtaining written, informed consent. All scans were performed using the pulse segments as the outermost loop of the acquisition. That is, the k-space data were fully sampled for a given pulse segment before acquiring data for subsequent segments.

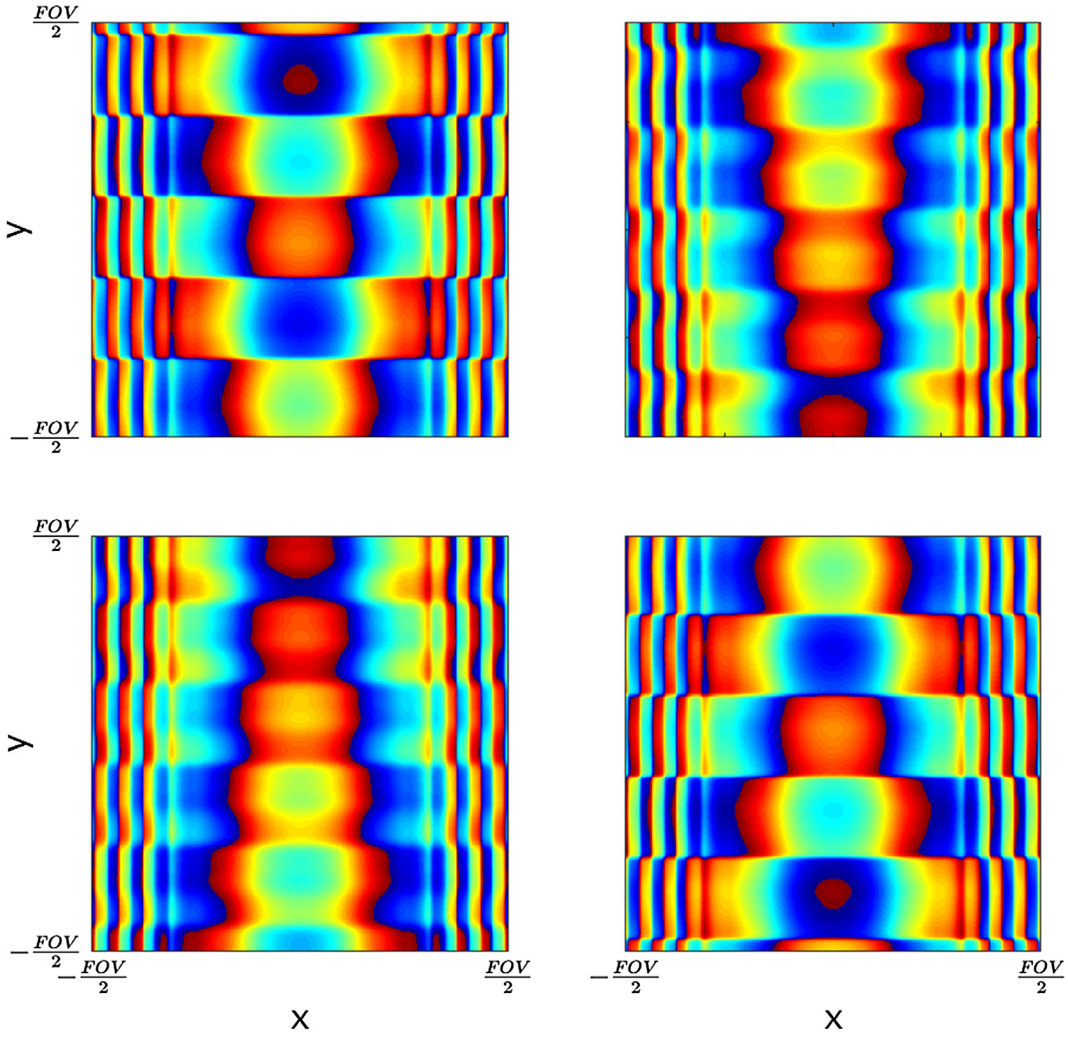

Fig. 2. The phase of the transverse magnetization for each of the 2D pulse segments when traversed in 4 segments.

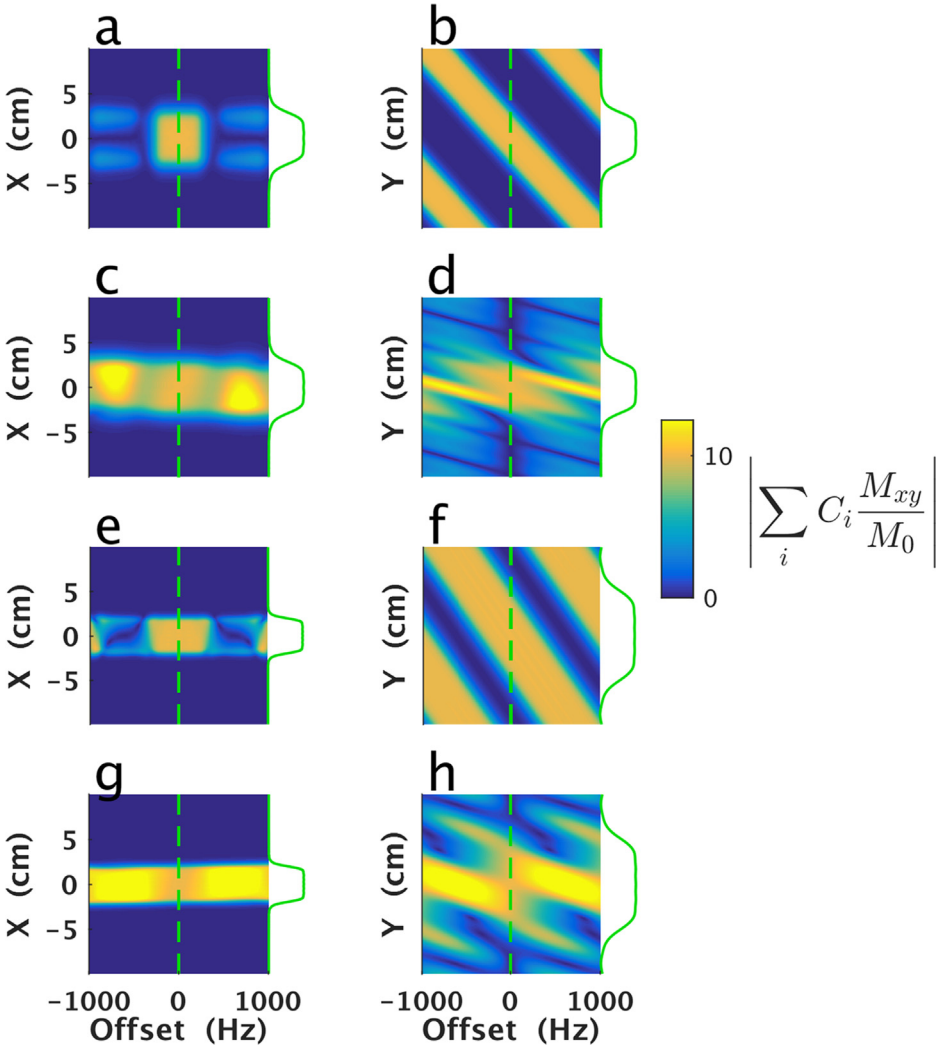

Fig. 3. Simulated excitation profiles produced by the 2D pulses used in experiments at 4T (a-d) and 3T (e-h), when performed without (a,b,e,f) and with segmentation (c,d,g, h). In all cases, the relative magnitude of the transverse magnetization is displayed as a function of position (x or y) versus resonance offset, for the case of flip angle equal 10° on resonance. As can be seen, the shape of the on-resonance excitation profile (green) is invariant with pulse segmentation. Coefficients C_i used in combining the data from the 4 shots (segmented pulses) are as defined in [1]. (For interpretation of the references to colour in this figure legend, the reader is referred to the web version of this article.)

4.1. 4T experiments

Two experiments were performed with a Varian DirectDrive console (Agilent Technologies, Santa Clara, CA) interfaced with a 4T, 90-cm magnet (Oxford Magnet Technology, Oxfordshire, UK) and a clinical gradient system (model SC72, Siemens, Erlangen, Germany). Experimental verification of the fully segmented and 4-segment imaging sequences was performed using the same pulse parameters as in [1] and as discussed in the Simulations section. Two experiments were performed to demonstrate the method at different levels of pulse segmentation. Both experiments were performed with a single channel transmit, single channel receive RF coil with Cartesian acquisition trajectories.

Gradient pre-emphasis was necessary on this system to prevent Nyquist ghosting of the excitation profile, which occurs when the positive and negative gradient lobes do not sample evenly about the center of k-space. Gradient pre-emphasis for the fast gradient was performed using the gradient impulse response function (GIRF) [18]. Therein, multiple triangular gradient waveforms of varying width and amplitude are measured on each gradient channel to fully sample the GIRF in the frequency domain. Gradient waveforms were measured following a protocol similar to Stich et al. [19], although here, 12 triangular waveforms were employed with amplitudes distributed linearly from 0.3125 G/cm to 3.75 G/cm. The slew rate of each waveform was set to 0.9 times the maximum possible to minimize waveform errors from the gradient amplifiers. The offset slice method [20] was used to measure the waveforms. In this method, a single 1-mm thick slice was offset 1.5 cm from isocenter for each gradient channel. The readout bandwidth was 50 kHz and the total readout time was 17 ms to obtain a spectral resolution of 58.82 Hz. Thirty averages were used with TR = 6 s and TE = 13.83 ms.

For the fully segmented sequence, a 3D T_1-weighted, spoiled GRE sequence was used with TR/TE = 6.09 ms/2.76 ms, flip angle = 10.4°, and receiver bandwidth = 100 kHz. Isotropic resolution of 1.5 mm^3 was used, with a FOV = 192 × 96 × 96 mm^3. The data acquired with 2D excitation were fully sampled experimentally and downsampled retrospectively to facilitate a comparison of SNR. For comparison, a non-selective excitation was used with FOV = 192 × 192 × 192 mm^3, matrix size = 192 × 192 × 192, while keeping the same TR, TE, flip angle, and acquisition bandwidth used in experiments deploying 2D pulses. The GRAPPA kernel was 3 × 2 × 3 in k_x, k_y, and k_z, respectively. Every 11th line of acquisition k-space was sampled in the slow dimension of the

pulse, which was phase encoded on readout. The center 6×32 lines of acquisition k-space were fully sampled in the phase-encoded dimensions (k_x and k_y) for use as autocalibrating signals (ACS). An elongated rectangle was employed to capture the maximal amount of signal energy for each pulse segment. The peak signal shifts in the slow dimension of the pulse when comparing different pulse segments, and the shape of the ACS region was designed to account for this. The ACS lines were used in the final reconstruction. The acceleration per pulse segment is $R = 7.341$ with the sampling pattern discussed and shown in Fig. 4. The acquisition time for the fully sampled dataset was approximately 11.64 min, while acquisition time for the accelerated readout (including the ACS data) would be approximately 1.59 min.

For the 4-segment excitation sequence, a 3D T_2^*-weighted, spoiled GRE sequence was performed using a flip angle of 10°, TR/TE = 41.5 ms/25 ms with one average. The receiver bandwidth was set at 100 kHz. Isotropic resolution of 1 mm was used, with a FOV = $192 \times 96 \times 96$ mm^3. Again, data were fully sampled experimentally and undersampled in processing. A reference image was acquired with the same TR, TE, flip angle, and bandwidth, but with FOV = $192 \times 192 \times 192$ mm^3 and 1 mm isotropic resolution. The GRAPPA kernel was again $3 \times 2 \times 3$ in k_x, k_y, and k_z, respectively, where every 3rd line of acquisition k-space was sampled in the slow dimension of the pulse. The center 40 lines of acquisition k-space were fully sampled in both phase-encoded dimensions for use as ACS data which were again used in the final reconstruction. The acceleration per segment in this case is $R = 1.882$, and the sampling pattern is shown in Fig. 5. The acquisition time for the fully sampled dataset was about 25.50 min and about 13.55 min for the undersampled readout, including the ACS data.

Noise prescans were measured at 4T using the same gain and receiver bandwidth as their respective imaging sequence, following the procedure in [21]. To obtain an accurate approximation of the noise standard deviation, 10^4 complex points were acquired in the absence of RF pulses. This yields an estimate of the noise standard deviation which is accurate to 1%, as described by Robson et al. [16]. As the pulse segments were acquired sequentially in time, there is no noise correlation between pulse segments. The pseudo-replica method [16] was used with 256 pseudo-replicas to calculate SNR and g-factor maps. The GRAPPA kernel was calculated once for the original undersampled k-space data and used in all following pseudo-replica images. For validation of the pseudo-replica results, the g -factor maps were also calculated using the method of Breuer et al. [22], where the g -factor is calculated directly from the GRAPPA kernel. The g -factors were compensated according to Eq. (13) of [22] to account for using the ACS data in the final reconstructions.

4.2. 3T experiments

An experiment was performed on a 3T Siemens Prisma scanner using a 32-channel head coil. A 2D HS1 pulse was designed using the second set of parameters presented in the Simulation section. This pulse was used for excitation in a 3D GRE EPI sequence, where

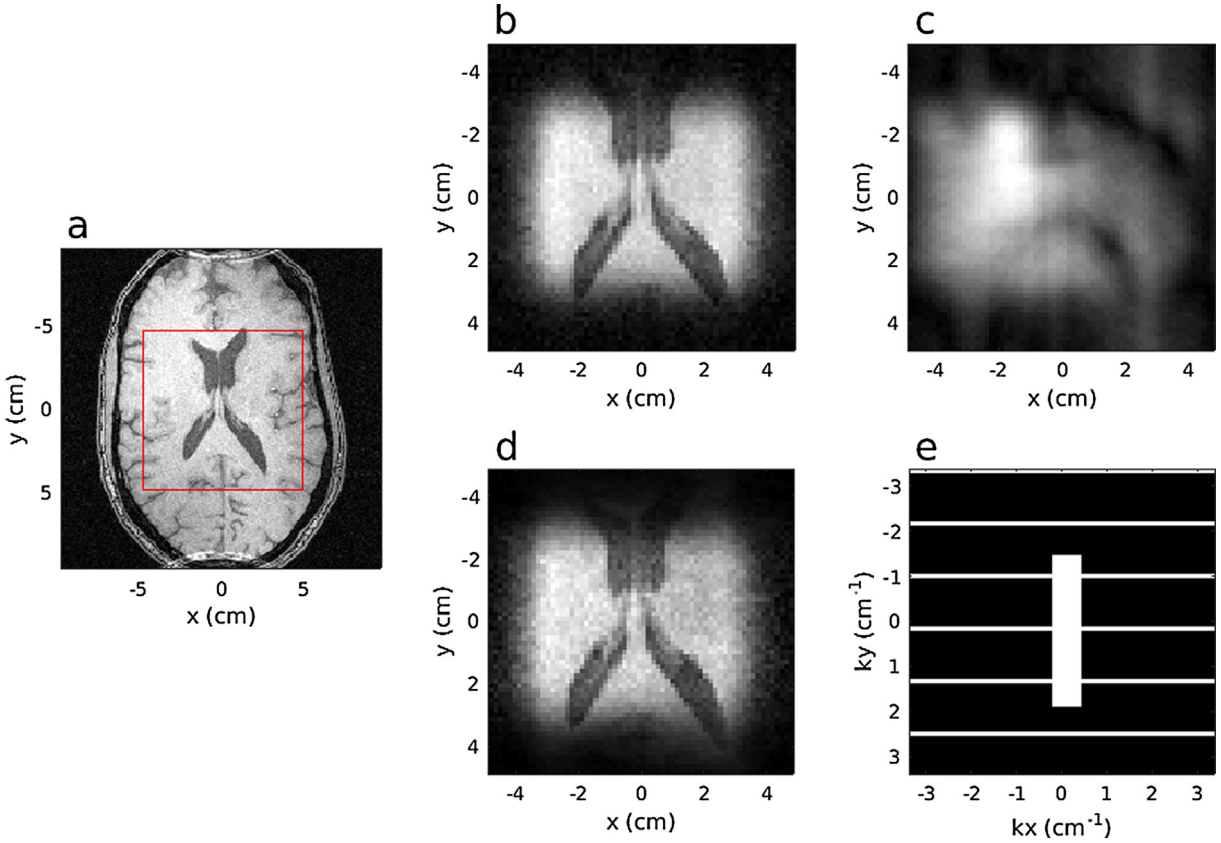

Fig. 4. Single plane from the 3D reconstructions of the fully segmented 2D HS1 pulse. Sequence parameters were TR = 6.09 ms, TE = 2.76 ms, FA = 10.4°, FOV = $96 \times 96 \times 192$ mm^3 with matrix size of $64 \times 64 \times 128$. (a) Reference image acquired with a non-selective excitation and FOV = $192 \times 192 \times 192$ mm^3 and matrix size of $192 \times 192 \times 192$, reconstructed using 3D FT. The red box indicates the zoomed FOV in the phase-encoded dimensions. (b) FT reconstruction of fully-sampled image data excited by the segmented 2D pulse. (c) FT reconstruction of undersampled image data, resulting in low resolution due to the center ACS region containing most of the signal energy. (d) GRAPPA reconstruction of the undersampled image data. (e) The retrospective undersampling pattern. White indicates sampled values, whereas black indicates unsampled. (For interpretation of the references to colour in this figure legend, the reader is referred to the web version of this article.)

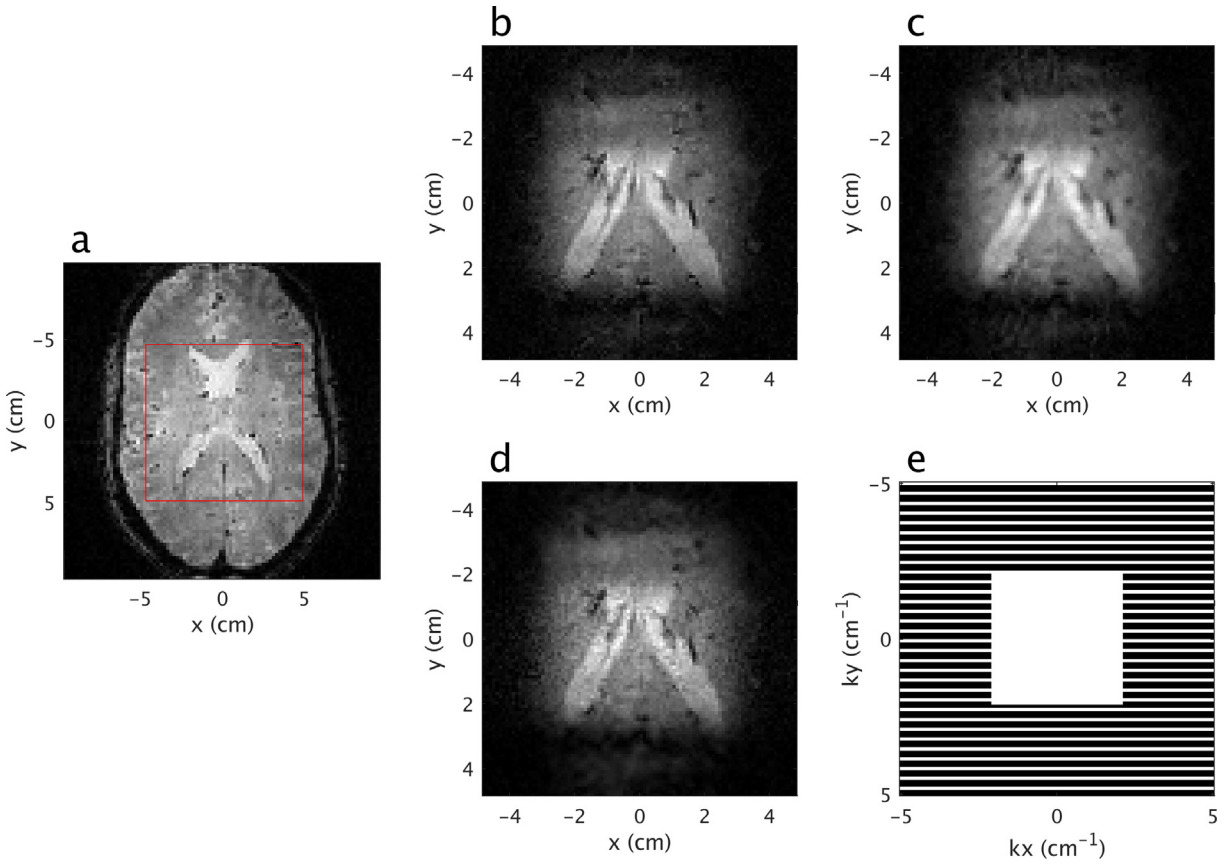

Fig. 5. Single plane from the 3D reconstructions of the 4-segment 2D HS1 pulse. Sequence parameters were TR = 41.5 ms, TE = 25 ms, flip angle = 10°, FOV = 96 × 96 x192 mm^3 with matrix size of 96 × 96 × 192. (a) Reference image acquired with a non-selective excitation and FOV = 192 × 192 × 192 mm^3 and matrix size of 192 × 192 × 192, reconstructed using 3D FT. The red box indicates the zoomed FOV in the phase-encoded dimensions. (b) FT reconstruction of fully-sampled image data excited by the segmented 2D pulse. (c) FT reconstruction of undersampled image data, resulting in low resolution due to the center ACS region containing most of the signal energy. (d) GRAPPA reconstruction of the undersampled image data. (e) The retrospective undersampling pattern. White indicates sampled values, whereas black indicates unsampled. (For interpretation of the references to colour in this figure legend, the reader is referred to the web version of this article.)

the phase-encoded dimensions were aligned with the spatially-selected dimensions of the 2D pulse. The sequence parameters were: TR/TE = 67 ms/19 ms, flip angle = 10°, FOV = 192 × 93 × 36 mm^3, and isotropic resolution of 1.5 mm. Data were fully sampled experimentally and undersampled in processing. The acquisition time for the fully sampled dataset was 12.9 s, while the acquisition for the accelerated dataset, not including ACS data, would have taken approximately 2.58 s. Gradient preemphasis was not necessary on this system.

The same GRAPPA kernel size was used here as at 4T, but now every 5th line of acquisition k-space was sampled in the slow dimension of the pulse. The central 16 lines of acquisition k-space were fully sampled in the phase-encoded dimension which was aligned with the segmented dimension of the pulse. All data along the fast dimension of the pulse was used as calibration data, as there were only 24 phase encodes in that direction. The ACS data were not used in the final reconstruction. The acceleration per segment in this case is $R = 5$, where the undersampling pattern is shown in Fig. 8. When combining the coil and pulse segment images, it is important to first perform a summation of the complex data over the pulse segments, since this combination is phase sensitive. The combination of coil data can then be performed in any desired manner, such as with sum-of-squares (SOS). In addition to using the pulse segments as virtual coils, reconstructions were also performed by first summing the pulse segments for each physical coil, followed by applying GRAPPA using only the physical coils for reconstruction.

5. Results

The results of a fully segmented pulse and 4-segment pulse at 4T are shown in Figs. 4 and 5, respectively. In both cases, a reference 3D gradient echo image is given with the same timing parameters and flip angle as the data using the associated 2D pulse. The direct Fourier reconstruction of the zero-filled undersampled data yields a low-resolution image dominated by the ACS energy. Using GRAPPA on the data from different pulse segments yields an image comparable in quality to the fully sampled reconstruction. For the 4-segment pulse, a small amount of residual blurring is visible around the periphery of the excitation profile.

The SNR and *g*-factor maps for the fully segmented pulse are shown in Fig. 6, while those for the 4-segment pulse are shown in Fig. 7. There is a modest loss of SNR for both cases. The *g*-factor map for the fully segmented pulse is spatially uniform within the excitation band of the pulse. For the 4-segment pulse, the *g*-factor map is non-uniform in space, being largest near the center of the profile and diminishing in magnitude near the edges of the profile in the slow dimension of the pulse. A discussion on the low values of the *g* -factor, particularly for the fully segmented pulse, is given in the Discussion section.

Reconstructions of 3T data using a 32-channel head coil are presented in Fig. 8. Again, the direct reconstruction of the undersampled data appears as an aliased, low resolution version of the fully sampled image. Except for some apparent noise amplification, the GRAPPA-reconstructed image recovers the lost resolution and

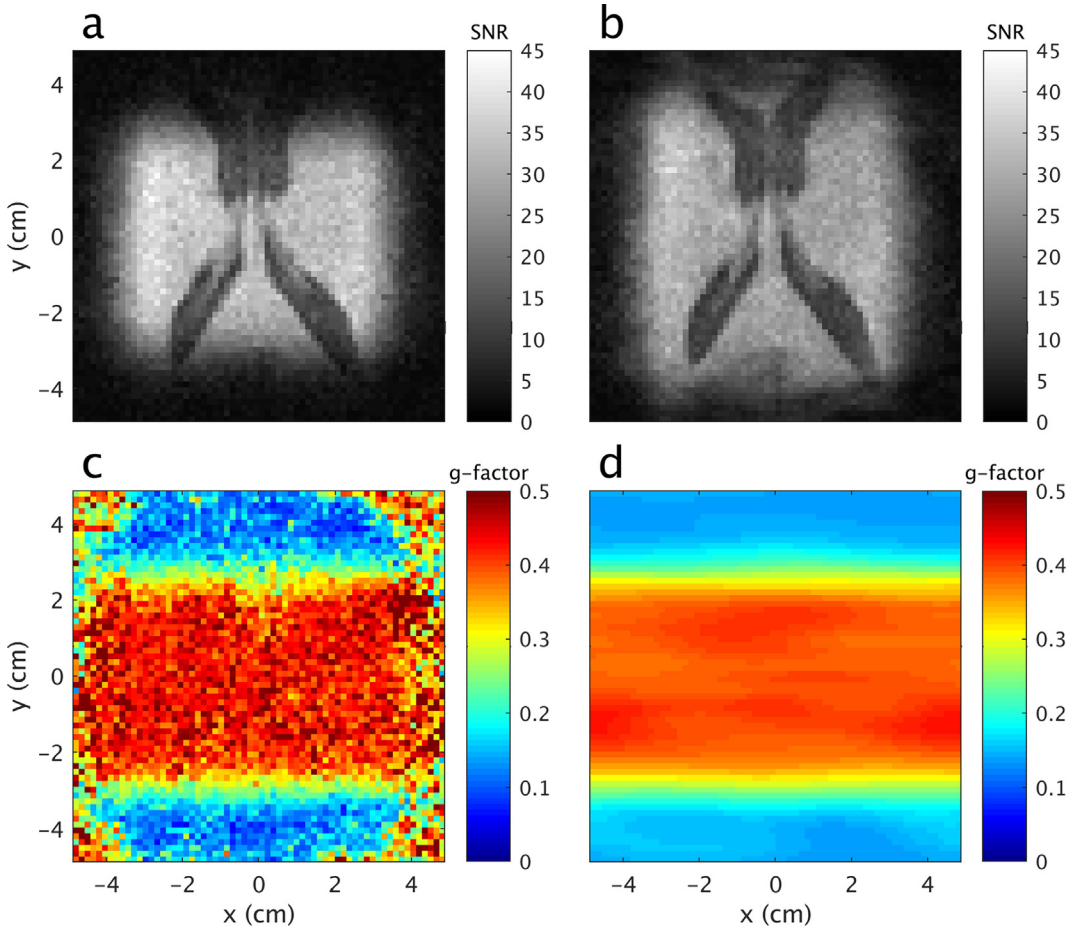

Fig. 6. SNR maps and *g*-factor map for the fully segmented excitation. (a) SNR map for the fully sampled readout, excited with the fully segmented 2D HS1 pulse. (b) SNR map for the undersampled data, showing a modest decrease in SNR. (c) The *g*-factor map calculated by the pseudo-replica method. (d) The *g*-factor map calculated directly from the GRAPPA kernel.

eliminates the aliasing due to data undersampling. SNR and *g*-factor maps were not calculated for the 3T data.

6. Discussion

While a segmented multidimensional pulse can provide greater tolerance to off-resonance effects as compared to its single-shot counterpart, the increased imaging time associated with segmentation can be a significant detriment. However, as shown herein, undersampling of acquisition k-space can be performed when using a segmented 2D pulse. Such undersampling can overcome the increased acquisition time associated with segmenting a 2D pulse, without significant detriment to the reconstructed images. As in the case of standard parallel imaging, the acceleration must not exceed the effective number of coils used. Due to limited spatial encoding with a small number of pulse segments, the degree of undersampling must be strictly less than the number of segments in some cases; otherwise, residual image aliasing persists.

The increased immunity to resonance offset, particularly in the fully-segmented case, is an appealing aspect of segmented multidimensional pulses. Indeed, Weber-Fahr et al. [8] applied a fully segmented pulse defined on a Cartesian trajectory to perform short-TE, single voxel spectroscopy with high resilience to B_0 inhomogeneity. There, the flip angle of the pulse was not increased at the periphery of k-space, followed by data scaling in processing, as was done in the present work. Qin et al. [7] applied a fully-segmented radial trajectory for a similar purpose to [8], which would likely benefit from a similar acceleration technique as presented here. Other applications include reduced FOV imaging with an EPI readout, whereby a 2D pulse permits a reduced FOV so that the EPI echo-train length can be shortened [10]. This lessens image distortions due to B_0 inhomogeneity. Segmenting the pulse in this scenario has the added benefit of reducing distortion of the excitation profile due to resonance offsets and permits a decreased minimum TE. 3D pulses have even longer durations than 2D pulses, further deteriorating pulse performance in the presence of resonance offsets.

As the pulse is segmented, the RF energy deposition increases, although by how much depends on the number of pulse segments. For ease of comparison, an equal TR and flip angle (10°) are used for each segment and compared to the single-shot case with the same parameters. For the 4-segment pulse, with a spatially varying flip angle, the peak flip angle within the magnetization profile for each segment is set to 10°. The first and fourth segments of the 4-segment pulse, which are equal in power by symmetry, deposit approximately 1.61-fold greater RF energy per unit time as the equivalent single-shot pulse. The second and third segments, which are also equal by symmetry, deposit approximately 1.23-fold greater RF energy per unit time as the single-shot pulse. For the fully segmented pulse, all segments are identical, and each segment deposits approximately 3.03-fold greater RF energy as the single-shot pulse per unit time.

Schneider et al. [9] and Jang et al. [23] employed parallel transmission (pTx) when employing 3D pulses for inner volume imaging to increase pulse performance. Applying pTx to shorten pulse dura-

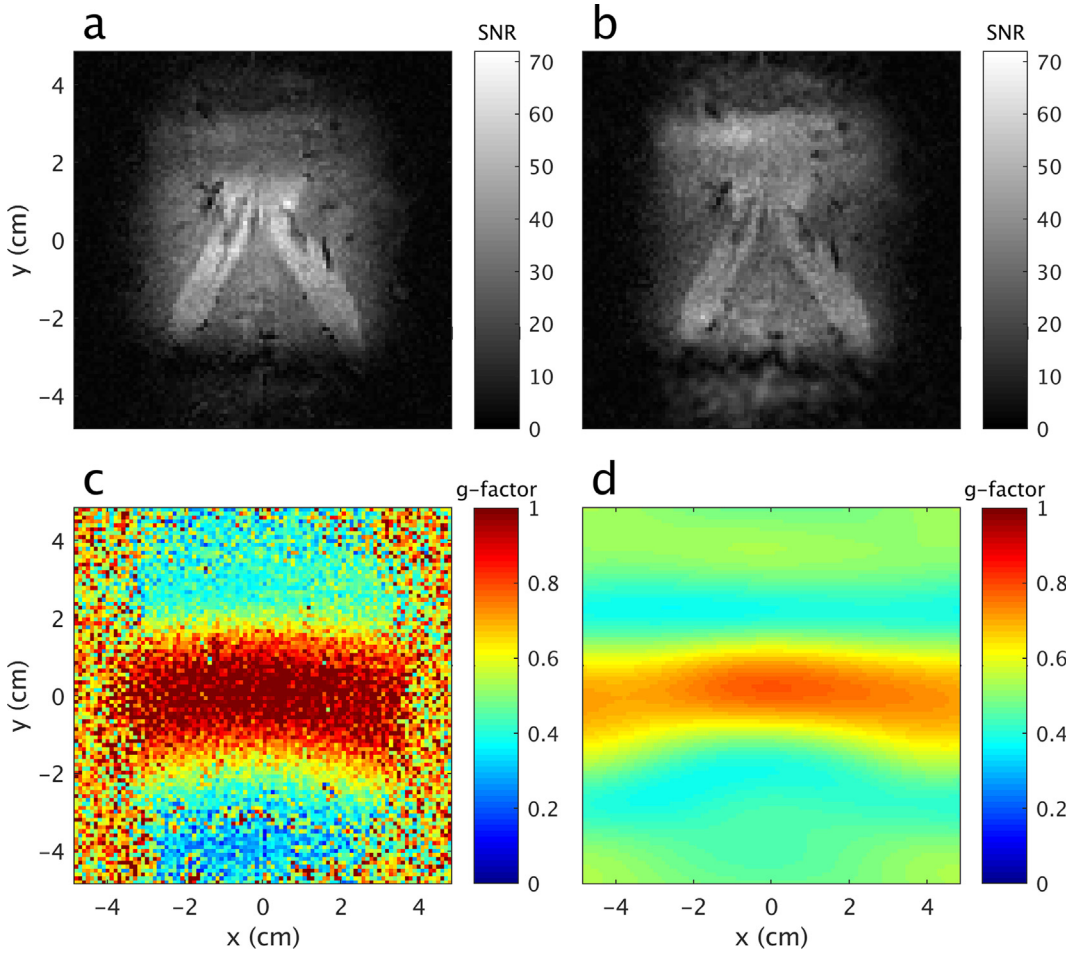

Fig. 7. SNR maps and *g*-factor map for the 4-segment excitation. (a) SNR map for the fully sampled readout, excited with the 4-segment 2D HS1 pulse. (b) SNR map for the undersampled data. (c) The *g*-factor map calculated by the pseudo-replica method. (d) The *g*-factor map calculated directly from the GRAPPA kernel.

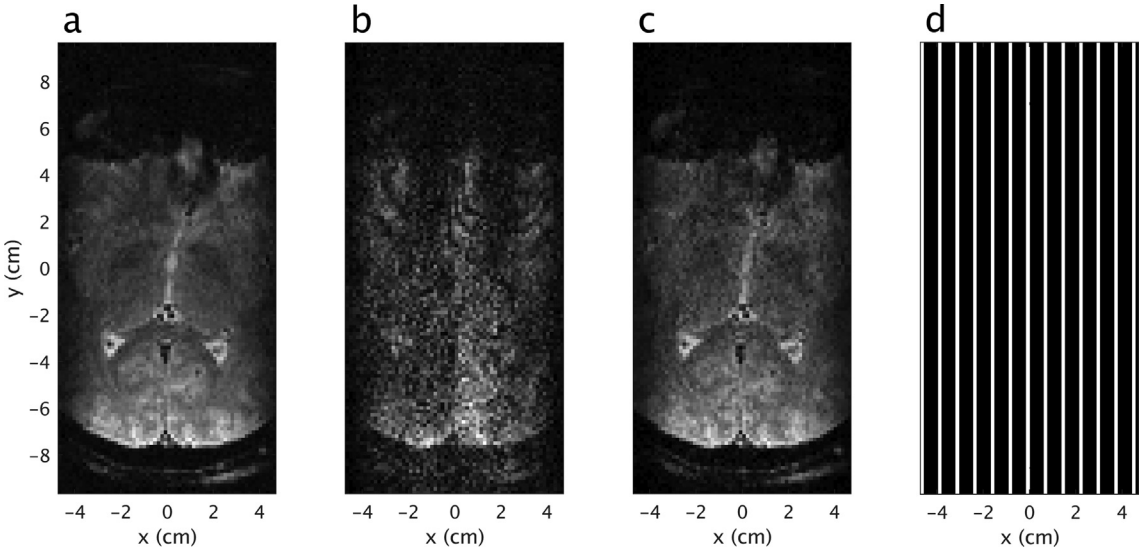

Fig. 8. Reconstruction of data from a 4-segment pulse when using a 32-channel receive coil in a 3D GRE EPI sequence. The readout direction is vertical, and the segmented direction of the pulse is horizontal. The horizontal direction was phase encoded during acquisition. (a) The fully sampled reconstruction. (b) GRAPPA reconstruction using only physical coils for GRAPPA after first summing over pulse segments. (c) GRAPPA reconstruction using each pulse segment as a virtual coil. (d) The undersampling pattern applied to the fully sampled data. White indicates sampled values, whereas black indicates unsampled.

tion is intrinsically different than the approach described herein. Excitation k-space is undersampled in pTx and the spatial information from multiple transmitters is used to compensate for the undersampling [24]. Here, the pulse is fully sampled when considering all segments of excitation k-space, while the acquisition is undersampled. Pulse segmentation and subsequent data undersampling could thus provide an alternative to parallel transmission on systems where such capabilities are not an option. In principle, this method could be extended to work with pTx such that the number of pulse segments is reduced.

Typically, *g*-factors are greater than unity, representing an amplification of noise due to the undersampling. Here, the fully segmented and 4-segment pulses used resulted in *g*-factors less than unity in many voxels. Such a result in the past has been argued to originate in the least-squares solution of the GRAPPA kernel weights, which conditions the noise in the reconstruction [16,25]. The *g* -factors in this work are significantly less than those found in previous studies, particularly for the fully segmented pulse; the underlying reason for this remains unknown. The *g* -factor maps were calculated by two different methods, pseudo-replica and directly from the GRAPPA kernel, in order to validate the numerical accuracy of this finding. Future efforts will investigate the origin(s) of the small *g* -factors found herein. However, the virtual coil sensitivities used in this work clearly differ in nature from the sensitivities of physical coils, which are typically greatest in magnitude near the coil and diminish quickly with distance. In light of these differences, future work will investigate the influence of the size of the ACS region on the *g* -factor map, or on how the choice of GRAPPA kernel affects the *g* -factor map.

Returning to a comparison with TIAMO [11], the transmitter in the present application is operated in a fixed mode, so there is no index over the transmit field map. In TIAMO, the transmitter is not operated in a fixed mode, so the transmit field map varies between acquisitions. The role of the varying transmit field map in TIAMO is replaced by the pulse segments in this work to achieve spatial encoding. Additionally, the different excitation modes used in TIAMO yield a varying flip angle between each excitation at a fixed spatial location. This non-ideality results in varying T_1-weighting and SNR at the same spatial location for each transmit mode. The present approach maintains consistent T_1 contrast and SNR with each excitation by using the same flip angle with every excitation segment. Finally, the present approach requires a complex summation over the excitation segments before combination of data from physical coils. This phase sensitive summation is not necessary in TIAMO.

In the spirit of reproducible research, all scripts to generate the in-vivo results in this paper can be found in the database [26].

7. Conclusions

We have presented a method for accelerating data acquisition when using segmented 2D RF pulses, which can likely be generalized to 3D pulses. We demonstrated the effects of noise amplification and have shown such amplification is approximately spatially uniform. We have also demonstrated the compatibility of the technique with conventional GRAPPA by treating all virtual and physical coil data as individual coils in the GRAPPA algorithm.

Acknowledgements

This work was supported by the National Institutes of Health grants U01 EB025153, P41 EB015894, and T32 EB008389. The authors would like to thank Drs. Steen Moeller and Gregor Adriany for useful discussions and for technical assistance and the reviewers for valuable recommendations to improve the clarity of the work.

References

[1] M. Mullen, N. Kobayashi, M. Garwood, Two-dimensional frequency-swept pulse with resilience to both B1 and B0 inhomogeneity, J. Magn. Reson. 299 (2019) 93–100.
[2] A. Jang, N. Kobayashi, S. Moeller, J.T. Vaughan, J. Zhang, M. Garwood, 2D Pulses using spatially dependent frequency sweeping, Magn. Reson. Med. 76 (5) (2016) 1364–1374.
[3] L.P. Panych, K. Oshio, Selection of high-definition 2D virtual profiles with multiple RF pulse excitations along interleaved echo-planar k-space trajectories, Magn. Reson. Med. 41 (2) (1999) 224–229.
[4] C.J. Hardy, P.A. Bottomley, 31P spectroscopic localization using pinwheel NMR excitation pulses, Magn. Reson. Med. 17 (2) (1991) 315–327.
[5] V.A. Stenger, F.E. Boada, D.C. Noll, Multishot 3D slice-select tailored RF pulses for MRI, Magn. Reson. Med. 48 (1) (2002) 157–165.
[6] D.G. Norris, P.J. Koopmans, R. Boyacioglu, M. Barth, Power independent of number of slices (PINS) radiofrequency pulses for low-power simultaneous multislice excitation, Magn. Reson. Med. 66 (5) (2011) 1234–1240.
[7] Q. Qin, J.C. Gore, M.D. Does, M.J. Avison, R.A. De Graaf, 2D Arbitrary Shape-Selective Excitation Summed Spectroscopy (ASSESS), vol. 58, 2007, pp. 19–26.
[8] W. Weber-fahr, M.G. Busch, J. Finsterbusch, Short-echo-time magnetic resonance spectroscopy of single voxel with arbitrary shape in the living human brain using segmented two-dimensional selective radiofrequency excitations based on a blipped-planar trajectory, Magn. Reson. Imaging 27 (5) (2009) 664–671.
[9] J.T. Schneider et al., Inner-volume imaging in vivo using three-dimensional parallel spatially selective excitation, Magn. Reson. Med. 69 (5) (2013) 1367–1378.
[10] N. Korn, J. Kurhanewicz, S. Banerjee, O. Starobinets, E. Saritas, S. Noworolski, Reduced-FOV excitation decreases susceptibility artifact in diffusion-weighted MRI with endorectal coil for prostate cancer detection, Magn. Reson. Imaging 33 (2015) 56–62.
[11] M.A. Griswold et al., Generalized autocalibrating partially parallel acquisitions (GRAPPA), Magn. Reson. Med. 47 (6) (2002) 1202–1210.
[12] M. Blaimer, M. Gutberlet, P. Kellman, F.A. Breuer, H. Köstler, M.A. Griswold, Virtual coil concept for improved parallel MRI employing conjugate symmetric signals, Magn. Reson. Med. 61 (1) (2009) 93–102.
[13] S. Orzada, S. Maderwald, B.A. Poser, A.K. Bitz, H.H. Quick, M.E. Ladd, RF excitation using time interleaved acquisition of modes (TIAMO) to address B1 inhomogeneity in high-field MRI, Magn. Reson. Med. 64 (2010) 327–333.
[14] J.M. Pauly, D.G. Nishimura, A. MacOvski, A k-space analysis of small-tip-angle excitation, J. Magn. Reson. 81 (1989) 43–56.
[15] M. Mullen, N. Kobayashi, M. Garwood, Corrigendum to 'Two-Dimensional frequency-swept pulse with resilience to both B1 and B0 inhomogeneity ' J. Magn. Reson. 299 (2019) 93–100, J. Magn. Reson. 305 (2019) 93.
[16] P.M. Robson, A.K. Grant, A.J. Madhuranthakam, R. Lattanzi, D.K. Sodickson, C.A. McKenzie, Comprehensive quantification of signal-to-noise ratio and g-factor for image-based and k-space-based parallel imaging reconstructions, Magn. Reson. Med. 60 (4) (2008) 895–907.
[17] B.A. Hargreaves, C.H. Cunningham, D.G. Nishimura, S.M. Conolly, Variable-rate selective excitation for rapid MRI sequences, Magn. Reson. Med. 52 (2004) 590–597.
[18] S.J. Vannesjo et al., Gradient system characterization by impulse response measurements with a dynamic field camera, Magn. Reson. Med. 69 (2) (2013) 583–593.
[19] M. Stich et al., Gradient waveform pre-emphasis based on the gradient system transfer function, Magn. Reson. Med. (2018) 1–12.
[20] J.H. Duyn, Y. Yang, J.A. Frank, J.W. van der Veen, Simple correction method for k-space trajectory deviations in MRI, J. Magn. Reson. 132 (1) (1998) 150–153.
[21] P. Kellman, E.R. McVeigh, Image reconstruction in SNR units: A general method for SNR measurement, Magn. Reson. Med. 54 (2005) 1439–1447.
[22] F.A. Breuer, S.A.R. Kannengiesser, M. Blaimer, N. Seiberlich, P.M. Jakob, M.A. Griswold, General formulation for quantitative G-factor calculation in GRAPPA reconstructions, Magn. Reson. Med. 62 (3) (2009) 739–746.
[23] A. Jang, X. Wu, E.J. Auerbach, M. Garwood, Designing 3D selective adiabatic radiofrequency pulses with single and parallel transmission, Magn. Reson. Med. 79 (2) (2018) 701–710.
[24] W. Grissom, C.Y. Yip, Z. Zhang, V.A. Stenger, J.A. Fessler, D.C. Noll, Spatial domain method for the design of RF pulses in multicoil parallel excitation, Magn. Reson. Med. 56 (3) (2006) 620–629.
[25] F.H. Lin, K.K. Kwong, J.W. Belliveau, L.L. Wald, Parallel imaging reconstruction using automatic regularization, Magn. Reson. Med. 51 (3) (2004) 559–567.
[26] Michael Mullen, Accelerated imaging with segmented 2D pulses using parallel imaging and virtual coils, Mendeley Data v1 (2019), http://dx.doi.org/10.17632/nr57j2fwcy.1.